

3D magnetic imaging using electron vortex beam microscopy

Frank Barrows ^{1,2}, Amanda K. Petford-Long^{1,2,3} & Charudatta Phatak ¹ 

Electron vortex beams are free-electron waves that carry orbital angular momentum. There has been growing theoretical and experimental interest in the use of electron vortex beams as a tool for the investigation of magnetic materials. However, due to the complex wavefront of the propagating waves, a deeper understanding of the interaction of electron vortex beams and the magnetic sample is needed. Here we calculate the magnetic phase shift that an electron vortex beam obtains upon transmitting through a magnetic sample. We show that this magnetic phase shift is influenced by the out-of-plane magnetization, which is a unique characteristic of incident electron vortex beams and is proportional to their orbital angular momentum. Finally, we develop a phase retrieval methodology to retrieve the out-of-plane component of magnetization. Based on our theory, we discuss suitable experimental conditions that would enable this imaging capability for magnetic materials and further extend to non-magnetic chiral materials.

¹Material Science Division, Argonne National Laboratory, Argonne, IL, USA. ²Applied Physics Program, Northwestern University, Evanston, IL, USA. ³Department of Materials Science and Engineering, Northwestern University, Evanston, IL, USA. ✉email: cd@anl.gov

The properties of magnetic materials are governed by the spatially varying three-dimensional spin texture within the material, which in turn is determined by the local energy landscape. Thus, in order to design and control the properties of new magnetic materials, it is particularly important to determine the three-dimensional map of the magnetization within magnetic materials^{1–3}. For example, there are a growing number of magnetic systems wherein a three-dimensional view of the magnetization is essential, such as Bloch skyrmions^{4,5}, hopfions⁶, and the magnetic spin structures in structured three-dimensional nanomagnets^{1,7}. Understanding the three-dimensional magnetization distribution of such systems is important both for basic science and for applications.

Currently, most microscopy methodologies are limited to imaging in two dimensions, leaving some components of the magnetic field invisible. In the case of surface-sensitive techniques such as magneto-optical Kerr microscopy, atomic force microscopy, and X-ray photoemission electron microscopy, the magnetization inside the sample is inaccessible^{8–10}. Transmission electron microscopy (TEM) remains the highest spatial resolution technique that can be used to reconstruct the components of the magnetic induction within and around a sample^{11,12}. Lorentz TEM and electron holography are both techniques that enable reconstruction of the magnetic field, i.e., magnetic induction. Thin-film TEM samples can be considered to have an in-plane component and an out-of-plane component of magnetic induction in the sample. The in-plane component is in the plane of the film (the xy -plane) and perpendicular to the direction of propagation of the electron beam down the microscope column (the z -axis). The out-of-plane component is perpendicular to the film and parallel to the direction of propagation of the electron wavefront.

Currently, there are only a few TEM-based techniques that can be used to reconstruct the out-of-plane component of the magnetic induction in a sample, such as magnetic circular dichroism and holographic vector field electron tomography^{13–16}. Magnetic circular dichroism is not widely adopted as the magnetic signal is detected in reciprocal space and producing spatially resolved maps requires specialized instruments including parallel beam illumination and electron energy loss spectroscopy. All other existing methodologies require acquiring a series of images with the sample at different tilt angles. As such, there are no techniques to image in real space the component of magnetization parallel to the incident beam and thus there are no techniques amenable to in situ experiments wherein the sample or beam cannot be tilted. The acquisition of a tilt series is tedious and thus not suitable for irreversible or stochastic processes, including magnetic phase transitions, furthermore a tilt series can be strongly influenced by diffraction contrast and is unsuitable when the sample is tilted into the magnetic field of the microscope lens in order to apply an external magnetic field across the sample¹⁷. Often times when performing in situ experiments, especially with samples requiring complicated experimental setups, e.g., liquid Helium cooled skyrmions¹⁸, the sample holder does not allow the acquisition of a tilt series. High-resolution imaging of the out-of-plane component of magnetization would have a range of applications, notably in the study of the out-of-plane magnetization in candidate spintronic and quantum computing materials^{19,20} such as skyrmions and skyrmion-based systems^{21,22}.

The advent of electron vortex beams (EVBs) provide an opportunity to develop tools to explore the spin structure of magnetic materials. Electron vortex beams are electron beams with a topologically non-trivial helical wavefront that carry orbital angular momentum (OAM). EVBs are of growing theoretical and experimental interest in their own right^{23–26}, and they have potential applications to the study of topological spin textures in

magnetic materials, for example through their use in electron energy loss magnetic chiral dichroism²⁷, via their interaction with magnetic fields through the Zeeman effect²⁸, through an OAM dependent focal length²⁹, through elastic scattering in EVB-based scanning transmission electron microscopy (STEM)^{30,31}, via manipulating magnetic nanoparticles³², and for determination of magnetic chirality³³ or crystal chirality^{34,35}. These beams have been realized experimentally by a number of means, including diffraction gratings^{24,25,36}, optical vortex beams³⁷, screw dislocations³⁸, magnetic monopoles^{39–41}, and artificial spin ices⁴². As the use of EVBs to characterize magnetic materials increases there is a need to develop a model that describes their interaction with realistic magnetic samples, i.e., samples with inhomogeneous magnetization; without such a model it is challenging to ensure that resulting images can be correctly interpreted. Previous work has demonstrated that EVBs gain a unique phase shift resulting from the out-of-plane magnetic induction due to a non-trivial OAM⁴³; this can be understood as resulting from the helical wavefront wherein the electron beam has a component perpendicular to an out-of-plane magnetic induction, B_z ^{43–45}. These analyses have focused on measuring the total phase shift but have not reconstructed an image of the out-of-plane component of magnetization. Further, these analyses have focused on the interaction with a uniform value of B_z , such that the magnetic vector potential, \mathbf{A} , is described by a simple analytical expression, namely the symmetric gauge⁴⁶. Currently, a general understanding of the electron phase shift imparted to topologically non-trivial wavefronts from the arbitrary magnetic fields in a realistic magnetic sample is lacking. Further, examining the phase of the EVB at the image plane in a TEM instrument, i.e., in the far-field, is non-trivial. There are numerous methods to model the contrast present in a defocused TEM image due to the phase shift imparted to the electron beam through interaction with the sample, i.e., Fresnel contrast^{47–49}. Unfortunately, the existing methods fail when both the intensity and the incident angle of the beam vary across the specimen, as in the case for EVBs^{47,50}.

Here we present a general approach to calculate the magnetic phase shift imparted to an EVB by an inhomogeneous magnetic field. We then simulate the Fresnel contrast in experimentally realizable TEM images. Finally, we describe a method to recover the magnetic phase shift from a set of images recorded using the EVBs. This work generalizes phase-reconstruction methodologies to topologically non-trivial wavefronts and has practical applications for Lorentz TEM, enabling a three-dimensional study of magnetic materials at the nanoscale. Our work goes beyond previous investigations to study magnetic samples that have magnetic induction, \mathbf{B} , with significant in-plane and out-of-plane components and that varies in orientation throughout the sample. Finally, we develop a phase-reconstruction methodology and demonstrate that the Fresnel contrast can be used to reconstruct a real space image of the out-of-plane component of the magnetic induction.

Results

Model for electron vortex beams. EVBs that have been physically realized in TEM are Laguerre Gaussian (LG) wavefunctions⁵¹. The LG wavefunctions propagate along and form a hyperbolic surface around the optic axis, the z -axis²⁴. The LG wavefunctions, Ψ that we have studied are characterized by the wavefunction^{43,52}

$$\Psi = \left[\frac{r}{w(z)} \right]^{|l|} L_n^{|l|} \left(\frac{2r^2}{w(z)^2} \right) e^{\left(\frac{-r^2}{w(z)^2} + \frac{ikr^2}{2R(z)} \right)} e^{i(l\phi + kz)} e^{-i(2n+|l|+1)\Xi(z)} \quad (1)$$

where k is the wavevector along the z -axis, r is the radius and ϕ is the polar angle in the xy -plane, and the direction of propagation

is in the positive z -direction down the transmission electron microscope column. $L_n^{|l|}$ are the generalized Laguerre polynomials with radial quantum number n and OAM quantum number l . $w(z)$ is the radius of the beam, defined as $w(z) = w_0 \sqrt{1 + z^2 z_R^{-2}}$, and w_0 is the radius of the beam when the EVB is narrowest, when $z=0$, i.e., the beam waist. z_R is the Rayleigh diffraction length, for the non-diffracting LG waves, $z_R = \frac{kw_0^2}{2}$, and $R(z) = z(1 + z^2 z_R^{-2})$ is the radius of curvature of the wavefronts. The Gouy phase, which is an additional phase shift of focused LG waves, is characterized by $\Xi(z) = \text{atan}(\frac{z}{z_R})$. Similar to previous experimental investigations^{24,25,53}, our work here focuses on EVBs with $n=0$. The intensity of the EVBs is annular in the xy -plane, and the radius of this annulus increases for larger quanta of OAM. The intensity does not depend on the sign of the OAM, but the LG wavefunction does propagate with a chiral wavefront which depends on the sign of the OAM.

In magnetic materials with an inhomogeneous magnetic induction, the corresponding magnetic phase shift imparted to the electron beam is influenced by the spatial variation of both the magnetic field and the EVB and we have set out to incorporate these effects into our model through the Aharonov Bohm (AB) effect^{54,55}. The AB effect describes the total phase shift, $\varphi(r)_{tot}$, of an electron wavefunction as a function of the electromagnetic potential in the sample along a path integral^{55,56}. It is worth noting that when the electrons are not strongly scattered from the sample it is appropriate to use a semi-classical path integral:⁵⁷

$$\varphi(\mathbf{r})_{tot} = \frac{\pi}{\lambda E} \int_L V(\mathbf{r}) dl - \frac{e}{\hbar} \int_L \mathbf{A}(\mathbf{r}) \cdot \hat{\omega} dl \quad (2)$$

Here the integration occurs along the direction of electron beam path given by the unit vector, $\hat{\omega}$ and along the curve l , the semi-classical path that an electron travels along, and E is the total energy of the electron. V and \mathbf{A} are the electrostatic and magnetic vector potentials, respectively, and each contributes to one of the two components of the total phase shift, namely the electrostatic phase shift, φ_E and the magnetic phase shift, φ_m . The focus of our investigation is the magnetic phase shift, φ_m , however, even in a purely magnetic sample there is a contribution to V from the sample, which is referred to as the mean-inner-potential.

In our investigation, we first demonstrate the phase shift the electron vortex beam obtains in magnetic fields analytically. We then use this information to determine the optimal conditions to maximize the signal in the TEM images and to motivate our reconstruction algorithm. We then demonstrate our reconstruction algorithm on simulated TEM images of several magnetic samples which is performed using a combination of micro-magnetic and finite-element simulations.

Semi-classical beam paths of electron vortex beams. In order to determine the magnetic phase shift imparted to an EVB we first need to determine the probability current in the vortex wavefront. This allows us to identify the semi-classical beam paths, which are then used to calculate the phase shift from the line integral in Eq. (2). Probability currents, \mathbf{j} , were calculated and used to construct semi-classical beam paths^{58,59}, see Supplementary Note 1 and 2 for details. We arrived at a time-dependent coordinate representation of the electron beam paths:

$$\mathbf{x}(s, \tau) = \begin{pmatrix} w_0 \sqrt{s^2 + 1} \cos(\tau) \\ w_0 \sqrt{s^2 + 1} \sin(\tau) \\ cs \end{pmatrix} \quad (3)$$

where $s = \frac{\hbar k}{z m_e} t$, $c = z_r$, and $\tau = \frac{1}{2} \text{atan}(s)$, and m_e is the relativistic electron mass. t is time, and here an initial position at $t=0$ is on

the beam waist, $r(t_0) = [x_0, y_0, 0]$. The expressions in Eq. (3) are hyperbolic trajectories that rotate around the optic axis. These hyperbolic trajectories diverge away from the beam waist, and wind in the xy -plane due to the non-trivial OAM. We have determined the semi-classical beam paths so that we can examine the magnetic phase shift that arises from the AB-effect, as detailed in the next section.

Calculating the magnetic phase shift. In this section we discuss a method to calculate the magnetic phase shift imparted to an EVB by a magnetic sample, and in the next section we will discuss the electrostatic phase shift. As an example, we investigate the magnetic phase shift, $\varphi_m(\mathbf{r})$, from a known magnetic vector potential, \mathbf{A} , using the beam paths described in Eq. (3). We investigated the phase shift resulting from a uniformly-magnetized spherical ferromagnetic nanoparticle of radius 20 nm, which is centered on the optic axis at the beam waist, $z=0$. A nanoparticle that is uniformly magnetized in the z -direction is characterized by the vector potential:⁶⁰

$$A_\phi = \frac{\mu_0}{3} M_0 r \sin(\theta) \quad (4)$$

where the magnetic vector potential is given in spherical coordinates defined by θ as the azimuthal angle, ϕ as the polar angle and r as the radius. A_ϕ is the nonzero component of the vector potential, μ_0 is the vacuum permeability, M_0 is the magnetization and r is the radial distance such that $r < \rho_0$, where ρ_0 is the radius of the nanoparticle. The magnetization is rotated away from the z -axis by an angle ν around the y -axis such that there is a component of the magnetization in the xy -plane⁶¹. This is shown schematically in Fig. 1a where we investigate nanoparticles with two different orientations of magnetization: $\nu = \frac{\pi}{6}$ and $\nu = \frac{5\pi}{6}$. The magnetic phase shift was found from Eq. (2), using a rotated vector potential (see Supplementary Note 3 for the rotated vector potential) and the EVB paths inside the sphere. As our investigation has focused on reconstructing the phase shift in TEM resulting from magnetic fields in ferromagnetic materials, the dominant contributions to the magnetic phase shift are due to the magnetization within the material⁶¹. The path integral is parameterized in time, from $-t_1$ to t_1 , which correspond to the times when the EVB is incident on and exits the nanoparticle, respectively. The magnetic phase shift separates into two distinct components due to the in-plane and out-of-plane components of the magnetization, as discussed in the Supplementary Note 4. Rewriting $\xi = \frac{-e\mu_0}{\hbar} M_0$ these two components of magnetic phase can be simplified to:

$$\varphi_{m_{xy}} = \xi \frac{\hbar k}{m_e} y t \Big|_{-t_1}^{t_1} \sin \nu \quad (5a)$$

$$\varphi_{m_z} = \xi \frac{\hbar l}{m_e} t \Big|_{-t_1}^{t_1} \cos \nu \quad (5b)$$

The total magnetic phase shift is then the sum of the phase shift resulting from the out-of-plane and in-plane components of magnetic induction, $\varphi_m = \varphi_{m_z} + \varphi_{m_{xy}}$. The limiting ratio of the phase shift resulting from B_z and from B_{xy} can be found:

$$\frac{\varphi_{m_z}}{\varphi_{m_{xy}}} = \frac{l}{ky} \cot(\nu) \quad (6)$$

The ratio of φ_{m_z} to $\varphi_{m_{xy}}$ is important; in order to map the out-of-plane component of magnetization, φ_{m_z} needs to be sufficiently large so as to be detected and separated from the typically larger value of $\varphi_{m_{xy}}$. From Eq. (6) this ratio can be seen to depend

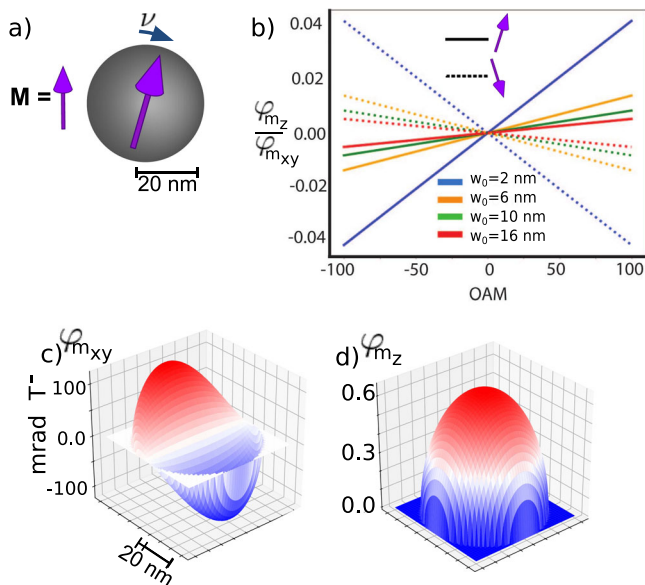


Fig. 1 The phase shifts from the in-plane and out-of-plane components of magnetization in a nanoparticle. **a** Schematic of a uniformly-magnetized nanoparticle, with \mathbf{M} the magnetization and $\nu = \frac{\pi}{6}$ is the angle the magnetization is rotated away from the z-axis. The magnetic phase shifts due to the out-of-plane and in-plane components of magnetization are indicated by φ_{m_z} and $\varphi_{m_{xy}}$, respectively. **b** Plot of the ratio of φ_{m_z} to $\varphi_{m_{xy}}$ imparted to the electron vortex beam (EVB) from a uniformly magnetized sphere rotated around the y-axis by $\frac{\pi}{6}$ (solid lines) and $\frac{5\pi}{6}$ (dashed lines). Different quanta of orbital angular momentum (OAM) are shown along the horizontal axis. Colors correspond to EVB paths with beam waists of w_0 . Plots of $\varphi_{m_{xy}}$ (**c**) and φ_{m_z} (**d**), which are the phase shift due to in-plane and out-of-plane magnetic induction, B_{xy} and B_z , respectively, in an EVB with OAM of 100. The phase shift per Tesla, mradT^{-1} , is normalized to the magnetic induction in the nanoparticle; the colors correspond to the phase shift per Tesla shown along the y-axis.

linearly on the OAM and inversely on both the distance along the y-axis at which the phase is measured and on the wavevector k , which corresponds to the electron beam energy. In Fig. 1b the ratio of φ_{m_z} to $\varphi_{m_{xy}}$ for the two configurations of the nanoparticle are shown in the solid and dashed lines, respectively, at an electron energy of 200 kV.

The y-dependence appears in Eq. (5a) because the nanoparticle was located at the beam waist and rotated around the y-axis, and thus the distance along the y-axis is, in effect, a measure of the radius of the beam waist perpendicular to the magnetic field. The ratio of φ_{m_z} to $\varphi_{m_{xy}}$ is larger closer to the optic axis, which is apparent for small values of w_0 in Fig. 1. At smaller values of r , the beam paths wind tightly around the optic axis, and thus the beam path has a larger component that is perpendicular to B_z .

For the uniformly-magnetized sphere, the ratio of φ_{m_z} to $\varphi_{m_{xy}}$ can be increased by centering the sample along the optic axis, (thus ensuring the distance from the optic axis is minimized), increasing the magnitude of the OAM, or by decreasing the beam energy. Notably, φ_{m_z} depends on the sign of the OAM, while $\varphi_{m_{xy}}$ does not.

Using Eq. (5a) and Eq. (5b) we calculated the magnetic phase shift imparted to an EVB with OAM of 100 by a uniformly-magnetized nanoparticle when $\nu = \frac{5\pi}{6}$. The $\varphi_{m_{xy}}$ and φ_{m_z} are shown in Fig. 1c, d respectively. We neglected the annular intensity in order to reconstruct the phase shift across the entire nanoparticle. $\varphi_{m_{xy}}$ agrees well with the calculated magnetic phase

shift reported in the literature⁶¹. φ_{m_z} appears to resemble the out-of-plane component of magnetization, which is largest at the center of the nanoparticle and is circularly symmetric. This demonstrates that φ_{m_z} and $\varphi_{m_{xy}}$ in an EVB can be calculated using the AB-effect. In the next section we build upon this work to present a method for computing images formed from EVBs.

Fresnel microscopy with electron vortex beams. To simulate images we first simulated the magnetic field in and around a magnetic sample using micromagnetic simulations and then calculated the magnetic phase shift from the simulated magnetic induction along the beam paths by using the finite element method (FEM), as described in the Methods Section. We demonstrate the accuracy of this method by comparing the analytical results for the magnetized nanoparticle with a simulated nanoparticle, see the Supplementary Note 5 for details of our implementation. Once the magnetic phase shift is calculated, the total phase shift was determined by adding the electrostatic phase shift calculated from the scalar potential V , representing the mean inner-potential of the sample. The electric phase shift imparted to an EVB can be calculated as $\varphi_E = \sigma V \tau$ where σ is the interaction constant dependent on the accelerating voltage of the electron microscope ($0.00728 \text{ rad V}^{-1} \text{ nm}^{-1}$ at 200 kV) and τ is the thickness of the sample. This simplification is valid when the paraxial Helmholtz approximation holds and when the sample has a uniform composition.

We simulated the TEM images generated from EVBs in order to demonstrate phase reconstruction of an arbitrary out-of-plane magnetization. When the paraxial Helmholtz approximation holds, the Fresnel contrast visible in a defocused image is described by¹¹:

$$I = |a\Psi e^{i\varphi_m} e^{i\varphi_E} \otimes T(r)|^2 \tag{7}$$

where a is the amplitude of the beam due to the presence of the sample and accounts for the loss of electrons as they are scattered outside the acceptance angle of the TEM projection lenses, Ψ is the EVB wavefunction incident on the sample, and $T(r)$ is the transfer function that is convolved with the exit wavefunction¹¹. The transfer function determines the defocus of the wavefunction at the image plane, and thus the Fresnel contrast in the image. In the simulations below, the sample sits below the beam waist, and thus the EVB is divergent and not strongly diffracting. Images are obtained from EVBs with small beam waists so as to increase the relative contribution of φ_{m_z} , Supplementary Note 5 describes how φ_{m_z} was simulated. Schematics of these conditions and the simulated TEM images are shown in Fig. 2.

In Fig. 2, the beam divergence and the helical wavefronts in an EVB are shown by the cone and colored paths, respectively; the color indicates the winding phase. The divergence of the beam is exaggerated in Fig. 2. In our simulations, the size of the beam waist and the distance between the sample and the beam waist are chosen so that the beam divergence is negligible within the thickness of the sample. In Lorentz-mode TEM, an objective mini-lens, OML, is used to focus the beam from the sample plane to the image plane. Figure 2a shows a beam focused without a sample present, and the intensity in the image plane is shown in (a.i). As can be seen, the conditions in (a.i) lead to the formation of an annular beam. To implement a reconstruction algorithm of the phase shift from an arbitrary magnetic induction, \mathbf{B} , near-uniform illumination across the simulated image is needed. Inversion algorithms to reconstruct the magnetization require spatial coherence of the illuminating beam^{62,63}. Thus, single images of EVBs are currently not well suited to a real-space reconstruction of the magnetization across the entire field of view.

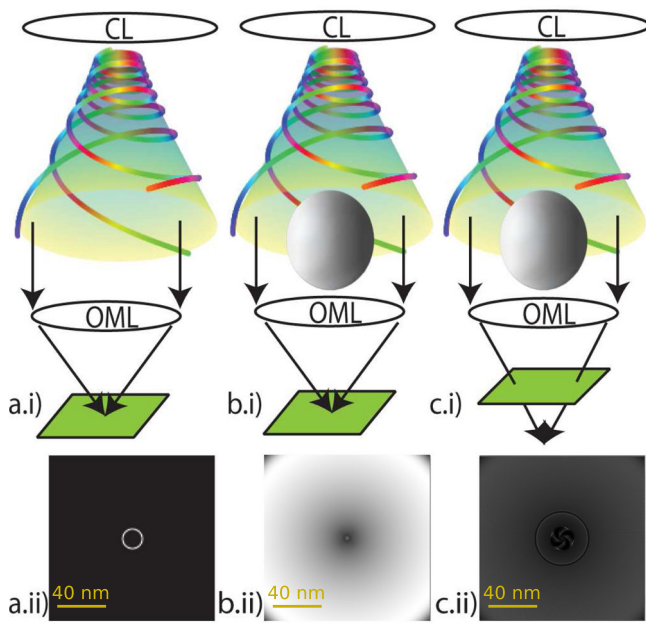


Fig. 2 **A schematic of Fresnel contrast obtained from electron vortex beams.** **a.i**, **b.i** and **c.i** schematics of the electron vortex beam (EVB) and electron beam configuration for three different defocus conditions. The EVB waist sits above the sample, so the beam is semi-convergent at the sample plane. The EVB waist is adjusted by the condenser lens (CL). The EVB divergence and the helical wavefronts are shown by the cone and colored paths, respectively: the color indicates the winding phase. The image focus is adjusted by the objective mini-lens (OML), which appears on a screen shown as the green plane. **a.ii** An in-focus image of the EVB without a sample. **b.ii** An in-focus image of an EVB and a nanoparticle sample, in order to obtain near-uniform illumination across the image, the simulated transmission electron microscopy (TEM) image in **b.ii** is a composite of multiple exposures, each acquired by adjusting the beam crossover-point and thus performing a longitudinal scan of the electron vortex beam over the sample. **c.ii** A defocused image of an EVB and a nanoparticle sample obtained by summing a series of images. In **b.ii** and **c.ii** the image is composed of multiple exposures obtained while adjusting the relative distance between the beam waist and the sample.

To achieve this our images are a summation of images, each acquired at a different position along the z -direction, and in each exposure a different portion of the sample is illuminated. The position along the z -direction would be adjusted experimentally by moving the beam crossover-point with respect to the sample plane, which is accomplished by changing the current of either the condenser lens (CL in Fig. 2), i.e., adjusting the beam spread, or the spherical-aberration corrector if present⁶⁴. Thus Eq. (7) is modified to include the distance from the beam waist to the sample, z_n :

$$I = \sum_n^N \left| a\Psi(z_n) e^{i\varphi_m} e^{i\varphi_E} \otimes T(r) \right|^2 \quad (8)$$

Figure 2b, c show images of a uniformly-magnetized nanoparticle with a 20 nm radius, obtained using Eq. (8) and an EVB with OAM=80. The simulated images shown in Fig. 2b.ii, c.ii are both sums of 50 different images with the distance from the beam waist to the sample plane ranging from 200 nm to 100 μm . The objective lens defocus is constant for all images that contribute to the series, in Fig. 2 b.ii, c.ii the OML defocus is 0 nm and 500 nm, respectively. Notably, in Fig. 2b.ii, c.ii there is decreased intensity at the corners of our simulations. This apparent four-fold symmetry is due to the finite size of our simulations and the

four corners of the simulated area, as a portion of the beam path is outside of the simulation, and thus the beam paths are poorly defined at these corners.

Phase reconstruction. In this section, we discuss the development of a phase-reconstruction approach to determine the phase shift due to the out-of-plane component of the magnetic induction. Our method is similar to the transport-of-intensity equation (TIE) approach developed by Teague et. al.⁶⁵, used to reconstruct the in-plane magnetization from the Fresnel contrast in a through-focal series of images. The key to our method is to utilize the dependence of the sign of φ_{m_z} on the sign of the OAM; the symmetry of this phase shift in EVBs with opposite OAM is utilized to overcome the challenge of reconstructing the phase of an EVB using the TIE^{66,67}. First, the analytical form of the wavefunction in the image plane needs to be determined; see the Supplementary Note 6 for a derivation of the image intensity I . While keeping all non-negligible terms up to second order in the objective lens defocus, Δf , and to second order in the electron wavelength, λ , the image intensity is given by the equation:

$$I = a^2 |\Psi|^2 + |\Psi|^2 \frac{\lambda \Delta f}{4\pi} \left[-2 \vec{\nabla}_\perp \cdot (a^2 \nabla_\perp \varphi_{tot}) - 2a \nabla_\perp a \cdot \left(\frac{2kr}{R(z)} \hat{r} + \frac{2l}{r} \hat{\phi} \right) - 2a^2 \nabla_\perp \varphi_{tot} \cdot \left(\frac{2l}{r} \hat{r} - \frac{4r}{w(z)^2} \hat{r} \right) - 2a^2 \left(\frac{2l|k}{R(z)} - \frac{4kr^2}{w(z)^2 R(z)} + \frac{2k}{R(z)} \right) + a |\Psi|^2 \frac{(\pi \Theta \Delta f)^2}{4\pi} \left[2(\nabla_\perp^2 a - (\nabla_\perp \varphi_{tot})^2 a) + 2 \nabla_\perp a \cdot \left(\frac{2l}{r} \hat{r} - \frac{4r}{w(z)^2} \hat{r} \right) - 2a \nabla_\perp \varphi_{tot} \cdot \left(\frac{2kr}{R(z)} \hat{r} + \frac{2l}{r} \hat{\phi} \right) + 2a \left(\frac{-4|l|}{w(z)^2} - \frac{4}{w(z)^2} + \frac{4r^2}{w(z)^4} - \frac{k^2 r^2}{R(z)^2} \right) + |\Psi|^2 \left(\left(\frac{\lambda \Delta f}{4\pi} \right)^2 + \left(\frac{\pi \Theta \Delta f}{4\pi} \right)^2 \right) \vec{\nabla}_\perp \cdot (a^2 \nabla_\perp \varphi_{tot}) \left(\frac{2k(|l|+1)}{R(z)} - \frac{4kr^2}{w(z)^2 R(z)} \right) + a^2 |\Psi|^2 \left(\left(\frac{\lambda \Delta f}{4\pi} \right)^2 + \left(\frac{\pi \Theta \Delta f}{4\pi} \right)^2 \right) \left[\frac{8|l|(|l|+1)k^2}{R(z)^2} - \frac{8(|l|+1)k^2 r^2}{w(z)^2 R(z)^2} + \frac{16|l|^2}{w(z)^4} + \frac{32|l|}{w(z)^4} - \frac{32|l|r^2}{w(z)^6} \right] \right] \quad (9)$$

We can further simplify the image intensity by accounting for the multiple exposures which produce an image, this is discussed in Supplementary Note 7. Here, Θ_0 is the beam divergence angle. In Fresnel-mode imaging with EVBs Θ_0 and Δf range from sub-milliradians to milliradians and nanometers to sub-millimeters, respectively. φ_{tot} depends on φ_m and φ_E , and φ_m depends on both φ_{m_z} and $\varphi_{m_{xy}}$. To isolate φ_{m_z} , we use images from two EVBs with opposite OAM, such as 100 and -100 , taken at the same defocus. Subtracting these two images gives:

$$I_{-l}(r, z, \Delta f) - I_{+l}(r, z, \Delta f) = |\Psi|^2 \frac{\lambda \Delta f}{\pi} \left[\frac{2al}{r} \nabla_\phi a + a^2 \nabla_r \varphi_{m_z} \left(\frac{2l}{r} - \frac{4r}{w(z)^2} \right) - \frac{\lambda \Delta f}{8\pi} \vec{\nabla}_\perp \cdot (a^2 \nabla_\perp \varphi_{m_z}) \left(\frac{2k(|l|+1)}{R(z)} - \frac{4kr^2}{w(z)^2 R(z)} \right) + \vec{\nabla}_\perp \cdot (a^2 \nabla_\perp \varphi_{m_z}) \right] + |\Psi|^2 \pi (\Theta_0 \Delta f)^2 \left[a^2 \nabla_r \varphi_{m_z} \frac{2kr}{R(z)} + a^2 (\nabla_\phi \varphi_{m_{xy}} + \nabla_\phi \varphi_E) \frac{2l}{r} + \frac{\pi}{8} (\Theta_0 \Delta f)^2 \vec{\nabla}_\perp \cdot (a^2 \nabla_\perp \varphi_{m_z}) \left(\frac{2k(|l|+1)}{R(z)} - \frac{4kr^2}{w(z)^2 R(z)} \right) \right] \quad (10)$$

Eq. (10) depends primarily on φ_{m_z} as contrast from the out-of-plane component of the magnetization will be additive upon subtracting the two images, while most of the contrast from the in-plane magnetization distribution and electrostatic phase shift should disappear. In Eq. (10) there is a contribution to the image contrast from the in-plane magnetization and from the electrostatic phase shift when it is multiplied by the OAM. To investigate the out-of-plane magnetization component we need to adjust our working conditions such that the in-plane magnetization and the

electrostatic phase shift do not contribute significantly to the image contrast. As discussed in the Supplementary Note 7, this can be achieved when the working conditions satisfy the following relation:

$$\frac{\Delta f}{w_0^2} \ll \frac{r}{2|l|\lambda} \frac{\nabla_{\perp}^2 \varphi_{m_z}}{\nabla_{\phi} \varphi_{m_{xy}} + \nabla_{\phi} \varphi_E} \quad (11)$$

As the electrostatic phase shift can be large compared to the magnetic phase shift, the phase reconstruction is optimized for homogeneous and flat samples wherein $\nabla_{\perp} \varphi_E$ would be negligible. In applying this condition in experiments, it is important to balance experimental conditions with useful information from the sample when r is very small, thus this condition may not be satisfied within a few nanometers of the beam waist, but this may be tolerable in a sample 10's of nanometers in size. We discuss below simple experimental methods to minimize the effect of the in-plane magnetization and the electrostatic potential.

Assuming that the microscope and beam conditions satisfy Eq. (11), or the simpler restriction for an unknown φ_m that $(\Theta_0 \Delta f)^2$ is small compared with $\lambda \Delta f$, then the contrast when taking the difference of images from two EVBs with opposite OAM can be approximated to depend solely on the out-of-plane magnetization.

Eq. (10) is written for a single image, but it can be generalized to data generated from multiple images, i.e., the images described by Eq. (8). In the implementation detailed below, the first, second and third terms within the first bracket of Eq. (10), which depends on $\lambda \Delta f$, are neglected. The first term within the brackets can be neglected when $\nabla_{\perp} a$ is negligible, i.e., when the amplitude is nearly uniform and the sample thickness does not vary significantly. We require that the lengthscale over which the amplitude varies is less than the lengthscale over which the out-of-plane magnetization varies, such that $\nabla_{\perp} a \ll \nabla_{\perp} \varphi_{m_z}$ and $(\nabla_{\perp} a^2) \cdot \nabla_{\perp} \varphi_{tot} \ll \nabla_{\perp}^2 \varphi_{m_z}$. The second and third terms are negligible as discussed in Supplementary Note 7. Similarly the second bracket of Eq. (10), which depends on $(\Theta_0 \Delta f)^2$, can be neglected when Eq. (11) is satisfied. Further the first and third terms in the second brackets are independently negligibly small, as discussed in Supplementary Note 7. We find that these approximations are justified when the gradient in the phase shift is much smaller than $0.1 \text{ rad} \cdot \text{nm}^{-1}$. These simplifications are valid in these simulations, and so Eq. (10) is rewritten:

$$\begin{aligned} \vec{\nabla}_{\perp} \cdot \left[\frac{I_{+l}(r, z, \Delta f) + I_{-l}(r, z, \Delta f)}{2} \nabla_{\perp} \varphi_{m_z}(r_{\perp}, \Delta f) \right] \\ \approx \frac{\pi}{\lambda} \left[\frac{I_{+l}(r, z, \Delta f) - I_{-l}(r, z, \Delta f)}{\Delta f} \right] \end{aligned} \quad (12)$$

Here the illumination of the electron beam is uniform across the image and we have averaged the two defocused images to approximate the modulus of the amplitude; the limitations of this approximation will be discussed below. This approximation is valid when $\Delta f \ll d^2/\lambda$ where d is the characteristic lengthscale over which the phase shift varies in the sample, as discussed in the Supplementary Note 7. This modified OAM-based TIE (OAM-TIE), Eq. (12), is a partial differential equation that can be used to solve for the phase shift.

We detail an alternative method to remove the contrast due to in-plane magnetization and the electrostatic potential in Eq. (10), for example when it is not possible to satisfy Eq. (11). By acquiring a pair of defocused images from EVBs with opposite OAM at opposite signs of defocus, i.e., two images $I_{+l}(r, z, -\Delta f)$, $I_{-l}(r, z, -\Delta f)$, it is possible to remove all terms from Eq. (10) that depend on Δf^2 , and thus effectively remove the contribution of Θ_0 . An alternative OAM-based TIE optimized for when Eq. (11)

is not satisfied is given by:

$$\begin{aligned} \vec{\nabla}_{\perp} \cdot \left[\frac{I_{+l}(r, z, \Delta f) + I_{-l}(r, z, \Delta f) + I_{+l}(r, z, -\Delta f) + I_{-l}(r, z, -\Delta f)}{2} \nabla_{\perp} \varphi_{m_z}(r_{\perp}, \Delta f) \right] \\ \approx \frac{\pi}{\lambda} \left[\frac{I_{+l}(r, z, \Delta f) - I_{-l}(r, z, \Delta f) - (I_{+l}(r, z, -\Delta f) - I_{-l}(r, z, -\Delta f))}{\Delta f} \right] \end{aligned} \quad (13)$$

The difference of images obtained when the microscope is over- and under-focused helps isolate the contrast due to the out-of-plane magnetization. On the left-hand side of Eq. (13) the average of images is again used to approximate the amplitude of the sample. We note that Eq. (13) is not well suited for in-situ experiments wherein matching overfocused and underfocused images can be difficult to obtain.

Application of the phase reconstruction. Here we implement the OAM-based TIE phase reconstruction detailed above to reconstruct the φ_{m_z} from two different samples. First, we tested our reconstruction algorithm on the two Permalloy ($\text{Ni}_{81}\text{Fe}_{19}$) magnetic nanoparticles discussed above. In Fig. 3a, b line plots of the simulated $\varphi_{m_{xy}}$ and φ_{m_z} for OAM of ± 20 and ± 100 are shown, respectively. In Fig. 3, the magnetic phase shift from nanoparticles with the out-of-plane magnetization oriented along the positive and negative z -directions are indicated with \uparrow and \downarrow , respectively. The plotted phase shift agrees well with the expected phase shift shown in Fig. 1c, d. As expected, φ_{m_z} depends on the sign of OAM in the EVB. Interestingly, $\varphi_{m_{xy}}$ does not depend on the sign of OAM when $l = \pm 20$ but it does when $l = \pm 100$, as seen by comparing the solid and dashed black lines in Fig. 3a, b. This is a result of a non-negligible contribution to the phase shift when $l = \pm 100$ due to the in-plane magnetization and the in-plane component of the helical beam paths when the sample is far from the beam waist. This means that the assumptions used to arrive at negligible $\varphi_{m_{xy}}$ in Eq. (10) is only valid for a certain range of OAM values. Thus we expect Eq. (12) and (13) to be valid for an OAM of ± 20 , but not for an OAM of ± 100 . This is discussed in more detail in the Supplementary Note 8, including a discussion of the parameter space in which Eq. (10) is valid.

The larger φ_{m_z} seen in Fig. 3a, b compared with that seen in Fig. 1 results from using a narrow beam waist. The phase shift was determined for an EVB with a beam waist of 0.5 nm, which has been experimentally realized⁵³. The phase shift and simulated images were created from sums of 100 different images with distance from the beam waist to the sample plane ranging from 10 nm to 100 μm . When implementing Eq. (12) the objective lens defocus was 50 nm, and when implementing the alternative phase reconstruction algorithm in Eq. (13) the objective lens defocus was 0.1 μm due to the weaker restriction of Δf .

Images used in the reconstruction were simulated with all three components of phase shift ($\varphi_{m_z}, \varphi_{m_{xy}}, \varphi_E$), but assuming ideality, the OAM-TIE approach will enable us to reconstruct φ_{m_z} . Figure 3c.i shows the simulated φ_{m_z} for an EVB with OAM=20, imparted by a nanoparticle with magnetization directed along the negative z -direction ($\nu = \frac{5\pi}{6}$) (indicated by superscript \downarrow) in grayscale, this is the ground truth φ_{m_z} . Figure 3c.ii-iii shows the reconstructed phase shift, indicated as φ^R , obtained using Eqs. (12) and (13), respectively. Images obtained using EVBs with OAM= +20 and -20 were used to implement the phase reconstruction, Eq. (12), the implementation of the phase reconstruction is discussed in the Methods Section. Figure 3d.i-iii show the simulated φ_{m_z} and reconstructed phase shifts, respectively, for a nanoparticle with magnetization directed along the positive z -direction ($\nu = \frac{\pi}{6}$) (indicated by superscript \uparrow) imaged with an EVB of OAM of ± 20 .

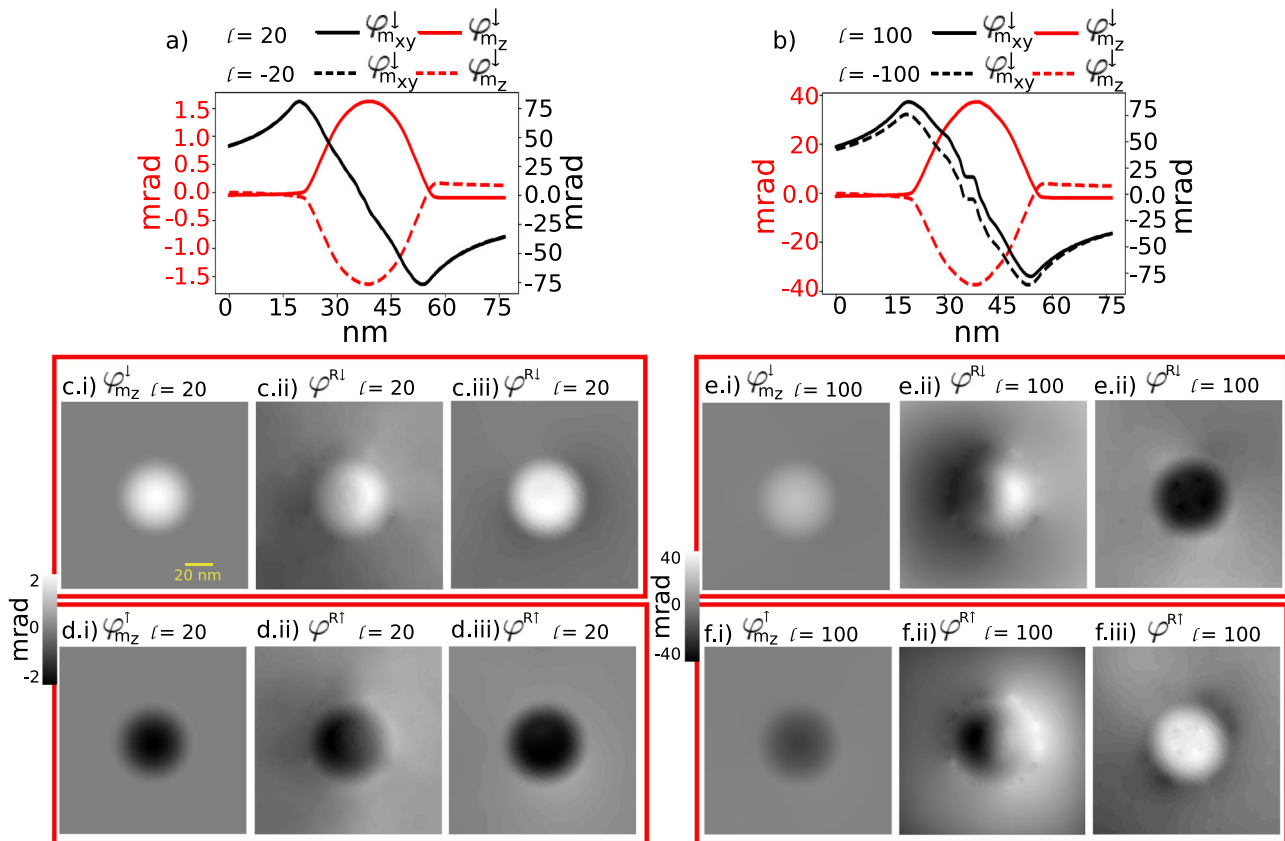


Fig. 3 Simulated phase shifts from a magnetic nanoparticle and implementation of the OAM-based transport-of-intensity equation (TIE). **a** and **b** Magnetic phase shifts from the in-plane component and out-of-plane component of magnetization, $\varphi_{m_{xy}}$ and φ_{m_z} , from a simulated Permalloy nanoparticle with orbital angular momentum (OAM) $l = \pm 20$ and $l = \pm 100$, respectively. The nanoparticle is oriented with the out-of-plane magnetization in the negative z -direction, indicated with the \downarrow superscript. The phase shifts, $\varphi_{m_z}^{\downarrow}$ and reconstructed phase shifts, φ^R , for the nanoparticle and shown in **c**, **d**, **e**, and **f**. Columns (i), (ii), and (iii) correspond to the simulation of the $\varphi_{m_z}^{\downarrow}$, the phase reconstructed from images obtained at a single defocus value, and the phase reconstructed from both overfused and underfused images; phase indicated by the color bars. **c** Phase shifts for electron vortex beam (EVB) with OAM=20 imparted by a nanoparticle with out-of-plane magnetization in the negative z -direction (\downarrow). **d** Phase shifts for EVB with OAM=20 imparted by a nanoparticle with out-of-plane magnetization in the positive z -direction (\uparrow). **e** Phase shifts for EVB with OAM =100 imparted by a nanoparticle with out-of-plane magnetization in the negative z -direction (\downarrow). **f** Phase shifts for EVB with OAM=100 imparted by a nanoparticle with out-of-plane magnetization in the positive z -direction (\uparrow).

The reconstruction reproduces the orientation of the φ_{m_z} as is evident when comparing Fig. 3c, d. There is quite good agreement between the reconstructed and simulated φ_{m_z} for an EVB with OAM=20, showing that φ_{m_z} can be isolated and reconstructed using the OAM-TIE method.

The OAM-TIE approach accurately reconstructs the φ_{m_z} , as seen by comparing Fig. 3c.ii, c.iii to c.i, ((d.ii), (d.iii) to (d.i)). We note that errors in the reconstructed phase in (c.ii) and (d.ii) are due to the in-plane magnetization and the electrostatic potential. The in-plane magnetization produces a slight dark to light gradient across the reconstructed phase while the electrostatic potential enhances the contrast from the edge of the sample. These effects are present in the reconstruction as the sample had significant in-plane magnetization and variation in sample thickness, and thus the effects of $\varphi_{m_{xy}}$ and φ_E could not be removed even when working with a small defocus of 50 nm. Comparing (c.ii) to (c.iii) ((d.ii) to (d.iii)) demonstrates the advantage that acquiring overfused and underfused images provides when working with samples that are not flat and which have significant in-plane magnetization. Noticeably, there is variation of the reconstructed phase outside of the nanoparticle, most apparent in (c.ii) and (d.ii), this is standard noise seen in reconstructions using the transport of intensity Eq⁶⁸.

Figure 3e.i–iii show the simulated φ_{m_z} and reconstructed phase shift, respectively, for a nanoparticle with magnetization directed along the negative z -direction imaged with an EVB of OAM of 100. The reconstructed phase in (e.ii) does not resemble φ_{m_z} , and varies from positive to negative values across the reconstruction. Thus the reconstructed phase resembles the known $\varphi_{m_{xy}}$, seen in Fig. 1c. This is a result of the dependence of $\varphi_{m_{xy}}$ on the sign of the OAM when $l = \pm 100$, as discussed above, and thus φ^R is a combination of the phase shifts resulting from both the in-plane and out-of-plane components of magnetic induction. Similarly in comparing Fig. 3f.i, ii the reconstructed phase resembles the $\varphi_{m_{xy}}$. In contrast (e.iii) and (f.iii) reconstructs φ_{m_z} well, though we note there is an asymmetric halo around the nanoparticle, we believe this is due to the in-plane magnetization, as discussed in Supplementary Note 8. Finally, we note that the circular symmetry of the magnetization contributes to the close correspondence between the simulated and reconstructed magnetic phase shifts; this is discussed in Supplementary Note 9.

We estimate the amount of time required to collect an image with sufficient signal to enable the reconstruction of the phase shift due to out-of-plane magnetization for the simulated nanoparticle. We assume a Gaussian noise distribution, and the

signal-to-noise ratio (SNR) can be written as $SNR = \bar{N}/\sqrt{\bar{N}}$ where \bar{N} is the average number of electrons per image pixel⁶⁹. φ_{m_z} corresponds to a milliradian phase shift which varies across tens of nanometers, thus from Eq. (9), the contrast due to φ_{m_z} should be 10^4 to 10^6 times smaller than the vortex beam intensity, depending on the defocus of the image, ranging from $10\ \mu\text{m}$ to $100\ \text{nm}$, respectively. As we would expect from Fig. 1, this is roughly 1000 times less intense than the contrast due to $\varphi_{m_{xy}}$, though notably sub-milliradian phase shifts have been resolved by electron holographic techniques while utilizing low current TEM⁷⁰. To resolve φ_{m_z} , the SNR needs to be less than the ratio of the phase shift to the beam intensity by at a minimum a factor of 2^{71} . Thus, assuming ideal conditions of beam current and coherence, a TEM with a conventional $1\ \text{nA}$ probe current would require between $10\ \text{s}$ and $1000\ \text{s}$ of total exposure across a 16-megapixel camera for a defocus of $1\ \mu\text{m}$ and $100\ \text{nm}$, respectively. The lower estimate of acquisition time is comparable to most TEM imaging. Thus each exposure in a longitudinal scan, wherein the EVB illuminates a portion of the frame, would require between a $0.1\ \text{s}$ and a $10\ \text{s}$ exposure.

The second example on which we tested the OAM-TIE reconstruction approach consists of a $180 \times 180 \times 20\ \text{nm}^3$ region of a ferromagnetic material that contains a stripe domain structure, representing a patterned square of a Co/Pd multilayer thin film with a perpendicular magnetic anisotropy^{72,73}. The in-plane and out-of-plane components of the magnetic induction are shown in Fig. 4a, b respectively. The orientation of the in-plane magnetic induction is indicated with the color wheel in (a), whereas the out-of-plane magnetic induction is shown in grayscale in (b). In Fig. 4 the positions of the domain walls are indicated with red dashed lines. Using conventional Lorentz TEM imaging the reconstruction of the magnetization would resemble Fig. 4a and the out-of-plane magnetization in these domains would be invisible.

In Fig. 4c the simulated phase shift resulting from the out-of-plane component of magnetic induction for an EVB with OAM of ± 20 is shown. As the chiral nature of the EVBs causes the

magnetic domains in φ_{m_z} to appear warped, φ_{m_z} shown in (c) is the average of the phase shift of EVBs with opposite chirality to make the domains easier to see. Therefore, the phase shift in (c) is $(\varphi_{m_z}^l - \varphi_{m_z}^r)/2$. $\varphi_{m_z}^l$ is multiplied by -1 as EVBs with opposite chirality will obtain a negative sign. The EVBs used to form the images had the same parameters as discussed above. The shift of the bright and dark domains relative to the red dashed lines at the edge of the samples, most noticeable at the corners, is an artifact of our simulation, see the Supplementary Note 5 for a further discussion of the origin of this artifact.

In Fig. 4d, e the reconstructed phase determined using Eqs. (12) and (13) are shown, respectively. Images used in the reconstruction were simulated with all three components of phase shift ($\varphi_{m_z}, \varphi_{m_{xy}}, \varphi_E$). The reconstructed phase in Fig. 4d, e both reproduces the general shape of the out-of-plane magnetization in the stripe domains in (b) and closely resembles the magnetic phase shift in (c). Comparing (d) and (e), we note the reconstructions are quite similar, which suggests that the phase reconstruction can be performed without obtaining both under-focused and overfocused images. We believe the differences between Fig. 4d, e are primarily due to the center of the vortex beam where there is little intensity, which is difficult to remove without comparing overfocused and underfocused images.

Discussion

In our investigation we have shown that the OAM-TIE approach can be used to reconstruct φ_{m_z} . In particular, φ_{m_z} can be reconstructed when the EVB parameters are such that the φ_{m_z} depends on the sign of OAM, but the $\varphi_{m_{xy}}$ does not. Most importantly, by modeling the expected magnetic phase shift, the parameter space in which this is true can be identified based on calculating the $\varphi_{m_{xy}}$ and φ_{m_z} , as we have done in Fig. 3a, b. Furthermore, examining Fig. 4b, d it is apparent that our phase reconstruction is able to isolate the phase shift resulting from the out-of-plane component of magnetic induction in a sample with multiple magnetic domains. Thus the OAM-TIE method is able to

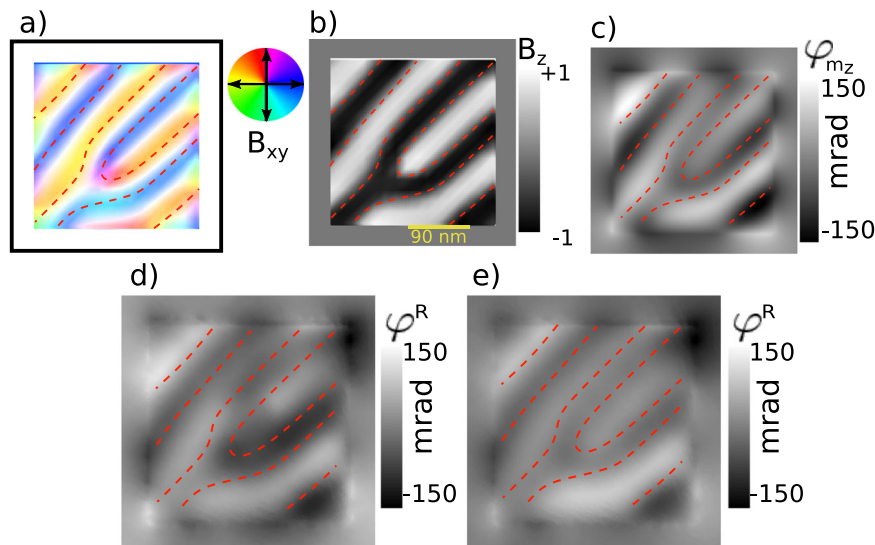


Fig. 4 Reconstruction of the phase shift resulting from the out-of-plane magnetic induction in a simulated sample with multiple domains. a The direction of in-plane magnetic induction, B_{xy} , indicated by the color wheel. **b** Out-of-plane magnetic induction, B_z , shown in gray-scale normalized to the magnetic saturation, indicated by the color bar. **c** Simulated magnetic phase shift due to the out-of-plane component of magnetization, φ_{m_z} , in an electron vortex beam (EVB) with orbital angular momentum (OAM) = ± 20 ; phase indicated by the color bars. **d** Phase shift reconstructed, $\varphi_{m_z}^R$, for EVB with OAM=20 obtained at a single defocus value. **e** Phase shift reconstructed for EVB with OAM=20 obtained using both overfocused and underfocused images.

reconstruct the local variations in out-of-plane magnetization that are otherwise inaccessible to reconstruction methodologies.

Thus, the OAM-TIE enables the reconstruction of a full field of view, and when coupled with the conventional TIE should be able to isolate the three-dimensional magnetization across a sample. The constraints on the spatial resolution of EVB based magnetic reconstruction will be comparable to conventional Lorentz TEM, up to 2 nm in dedicated machines⁷⁴, and thus EVB based microscopy will be a powerful technique to image the real space out-of-plane component of magnetization. Furthermore, the OAM-TIE can be implemented in most electron microscopes, as it does not necessitate a specialized STEM mode or a fast in-situ camera. Additionally, compared to STEM-based techniques that quantify the magnetic flux through the electron vortex beam, including electron vortex beam holography and interferometric based approaches^{46,75}, the OAM-TIE should provide better spatial resolution by acquiring a full field reconstruction of the magnetic phase shift. Further, holography and interferometric based techniques require a reference wave, whereas the OAM-TIE in principle does not and can be implemented anywhere across a sample.

Further work is needed in order to quantify the out-of-plane component of the magnetization from the reconstructed magnetic phase shift, currently only the phase shift resulting from the out-of-plane component of magnetization can be reconstructed quantitatively. A source of error in the OAM-TIE is approximating the in-focus image by the average of two defocused images with opposite OAM. This was done to minimize artifacts from the multiple exposures in a single image, but it introduced errors due to the presence of Fresnel contrast from the $\varphi_{m_{xy}}$ and may introduce experimental errors when the paraxial Helmholtz approximation is not perfectly satisfied and the Gouy phase introduces non-negligible contrast. Future work should focus on implementing the OAM-TIE with an in-focus image, which may minimize these errors. Additionally, in arriving at Eq. (12) we neglected spatial variation in the amplitude of the wavefunction, but in samples with varying thickness there will be a non-negligible gradient in the amplitude. While we were able to implement OAM-TIE on a nanoparticle, accounting for variation in the amplitude is required to fully generalize this work. Further, developments in phase reconstruction methodologies that can be implemented on images obtained without fully illuminated fields of view, such as a single EVB acquisition, could enable an OAM-based real space reconstruction of the magnetic phase shift at individual positions during a transverse scan of the electron beam. A transverse scan of the EVB would be amenable to standard STEM workflows and would likely minimize sources of experimental error such as variations in the beam position, including beam drift, while enabling the reconstruction of the magnetization at the center of the vortex.

Conclusion

We have developed a generalized method to simulate the phase shift imparted by a magnetic sample to an electron vortex beam and introduced a phase retrieval algorithm for reconstructing the phase shift resulting from the out-of-plane component of magnetic induction. This has implications for the study of magnetic materials as well as the study of electron vortex beams. We have shown both analytically and numerically that electron vortex beams with non-zero OAM gain a magnetic phase shift from an out-of-plane magnetization. Finally, we demonstrated our phase retrieval algorithm for experimentally realizable conditions and identified advancements in the design of EVBs, particularly narrow beam waists, that will enable more robust implementations of EVB based phase microscopy. By establishing a methodology to

reconstruct the out-of-plane component of magnetization a complete reconstruction of the magnetization in a magnetic material is possible in combination with conventional Lorentz TEM. Further work is needed to generalize this work to chiral materials wherein the electrostatic phase shift may depend on the sign of the OAM.

Methods

All simulations were implemented using the finite element method (FEM); in the FEM a mesh space composed of simplices is built to solve partial differential equations. The FEM was used to simulate magnetic materials, calculate the magnetic phase shift in the EVB, and implement the phase reconstruction algorithm. Magnetic materials were simulated using the micromagnetic package Fimmag⁷⁶. The magnetic ground state for the magnetic samples was found by relaxing the magnetic configuration from an initial in-plane or out-of-plane magnetization, the magnetic nanoparticle was modeled with a magnetic saturation of $3.8 \times 10^5 \text{ Am}^{-1}$, an exchange stiffness of $8.7 \times 10^{-12} \text{ Jm}^{-1}$, while the thin film was modeled with a magnetic saturation of $8.6 \times 10^5 \text{ Am}^{-1}$, an exchange stiffness of $1.3 \times 10^{-11} \text{ Jm}^{-1}$, and a Dzyaloshinskii-Moriya interaction of $4 \times 10^{-3} \text{ Jm}^{-2}$. In the nanoparticle simulations, a mesh space of $70 \times 70 \times 20$ elements was used, representing a $90 \times 90 \times 50 \text{ nm}^3$ space. In the thin film simulations, a mesh space of $70 \times 70 \times 20$ elements was used, representing a $180 \times 180 \times 50 \text{ nm}^3$ space. Our simulations were performed such that there was sufficient vacuum space around the sample that Dirichlet boundary conditions were implemented on all the mesh boundaries.

Modeling the phase shift and implementing the phase reconstruction algorithm were performed using the FEniCS package⁷⁷, the simulated magnetic fields were interpolated directly into a FEniCS mesh space. The magnetic phase shift of the exit wavefunction was determined along the calculated electron beam paths as discussed in the Supplementary Note 5, and the beam path was determined using Eq. (3). For the nanoparticle, the magnetic phase shift was calculated at 20 partitions along the z -axis of the rectangular mesh of $70 \times 70 \times 20$ elements, each was projected into a 256×256 mesh representing a $130 \times 130 \times 2.5 \text{ nm}^3$ space. For the thin film, the magnetic phase shift was calculated at 20 partitions along the z -axis of the rectangular mesh of $70 \times 70 \times 20$ elements, each was projected into a 512×512 mesh representing a $380 \times 380 \times 2.5 \text{ nm}^3$ space. We implemented Dirichlet boundary conditions on all the mesh boundaries as the phase shift at the boundaries of the mesh is negligible.

The total phase shift was determined by adding to the magnetic phase shift the electrostatic phase shift, the electrostatic phase shift was calculated by projecting the thickness of the sample along the z -direction to determine the thickness τ , and the scalar potential V was 25 V ^{12,78}. The phase reconstruction was performed by implementing Eq. (12) using defocused images which were interpolated into a 256×256 mesh representing a $256 \times 256 \text{ nm}^2$ space. A mask 5 nm in diameter was applied to the center of the images to minimize artifacts due to the lack of intensity along the optic axis, and Dirichlet boundary conditions of zero phase shift are set on the edge of the images.

Data availability

The data that support the findings of this study are available from the corresponding author upon reasonable request.

Code availability

The codes used for simulations that support the findings of this study are available from the corresponding author upon request.

Received: 29 October 2021; Accepted: 9 November 2022;

Published online: 12 December 2022

References

1. Fernández-Pacheco, A. et al. Three-dimensional nanomagnetism. *Nat. Commun.* **8**, 15756 (2017).
2. Manke, I. et al. Three-dimensional imaging of magnetic domains. *Nat. Commun.* **1**, 125 (2010).
3. Tang, J. et al. Two-dimensional characterization of three-dimensional magnetic bubbles in Fe_3Sn_2 nanostructures. *National Science Review* **8** (2020).
4. Rybakov, F. N., Borisov, A. B., Blügel, S. & Kiselev, N. S. New spiral state and skyrmion lattice in 3d model of chiral magnets. *N. J. Phys.* **18**, 045002 (2016).
5. Zhang, S. et al. Reciprocal space tomography of 3d skyrmion lattice order in a chiral magnet. *Proc. Nat. Acad. Sci.* **115**, 6386–6391 (2018).
6. Kent, N. et al. Creation and observation of hopfions in magnetic multilayer systems. *Nat. Commun.* **12**, 1562 (2021).

7. Sanz-Hernández, D. et al. Fabrication, detection, and operation of a three-dimensional nanomagnetic conduit. *ACS Nano* **11**, 11066–11073 (2017).
8. Urs, N. O. et al. Advanced magneto-optical microscopy: Imaging from picoseconds to centimeters - imaging spin waves and temperature distributions (invited). *AIP Adv.* **6**, 055605 (2016).
9. Abelmann, L. Magnetic force microscopy. In Lindon, J. C., Tranter, G. E. & Koppenaal, D. W. (eds.) *Encyclopedia of Spectroscopy and Spectrometry (Third Edition)*, 675–684 (Academic Press, Oxford, 2017), third edition edn.
10. Locatelli, A. & Menteş, T. O. Chemical and Magnetic Imaging with X-Ray Photoemission Electron Microscopy, 571–591 (Springer Berlin Heidelberg, Berlin, Heidelberg, 2015).
11. De Graef, M. Introduction to Conventional Transmission Electron Microscopy (Cambridge University Press, 2003).
12. Dunin-Borkowski, R., Kovács, A., Kasama, T., McCartney, M. & Smith, D. Electron Holography, chap. 16, 767–818 (Springer Handbooks. Springer, Cham., 2019).
13. Phatak, C., Beleggia, M. & De Graef, M. Vector field electron tomography of magnetic materials: Theoretical development. *Ultramicroscopy* **108**, 503–513 (2008).
14. Wolf, D. et al. Holographic vector field electron tomography of three-dimensional nanomagnets. *Commun. Phys.* **2**, 87 (2019).
15. Schattschneider, P. et al. Detection of magnetic circular dichroism using a transmission electron microscope. *Nature* **441**, 486–488 (2006).
16. Wang, Z. et al. Atomic scale imaging of magnetic circular dichroism by achromatic electron microscopy. *Nat. Mater.* **17**, 221–225 (2018).
17. Taheri, M. L. et al. Current status and future directions for in situ transmission electron microscopy. *Ultramicroscopy* **170**, 86–95 (2016).
18. Yu, X. et al. Real-space observations of 60-nm skyrmion dynamics in an insulating magnet under low heat flow. *Nat. Commun.* **12**, 5079 (2021).
19. Kent, A. D. Perpendicular all the way. *Nat. Mater.* **9**, 699–700 (2010).
20. Psaroudaki, C. & Panagopoulos, C. Skyrmion qubits: A new class of quantum logic elements based on nanoscale magnetization. *Phys. Rev. Lett.* **127**, 067201 (2021).
21. Jiang, W. et al. Physical reservoir computing using magnetic skyrmion memristor and spin torque nano-oscillator. *Appl. Phys. Lett.* **115**, 192403 (2019).
22. Song, K. M. et al. Skyrmion-based artificial synapses for neuromorphic computing. *Nat. Electron.* **3**, 148–155 (2020).
23. Negi, D. S., Idrobo, J. C. & Ruz, J. Probing the localization of magnetic dichroism by atomic-size astigmatic and vortex electron beams. *Sci. Rep.* **8**, 4019 (2018).
24. McMorran, B. J. et al. Electron vortex beams with high quanta of orbital angular momentum. *Science* **331**, 192–195 (2011).
25. Verbeeck, J., Tian, H. & Schattschneider, P. Production and application of electron vortex beams. *Nature* **467**, 301–304 (2010).
26. Bandyopadhyay, P., Basu, B. & Chowdhury, D. Geometric phase and fractional orbital-angular-momentum states in electron vortex beams. *Phys. Rev. A* **95**, 013821 (2017).
27. Schattschneider, P., Löffler, S., Stöger-Pollach, M. & Verbeeck, J. Is magnetic chiral dichroism feasible with electron vortices? *Ultramicroscopy* **136**, 81–85 (2014).
28. Guzzinati, G., Schattschneider, P., Bliokh, K. Y., Nori, F. & Verbeeck, J. Observation of the larmor and gouy rotations with electron vortex beams. *Phys. Rev. Lett.* **110**, 093601 (2013).
29. Harvey, T. R., Grillo, V. & McMorran, B. J. Stern-gerlach-like approach to electron orbital angular momentum measurement. *Phys. Rev. A* **95**, 021801 (2017).
30. Edström, A., Lubk, A. & Ruz, J. Elastic scattering of electron vortex beams in magnetic matter. *Phys. Rev. Lett.* **116**, 127203 (2016).
31. Edström, A., Lubk, A. & Ruz, J. Magnetic effects in the paraxial regime of elastic electron scattering. *Phys. Rev. B* **94**, 174414 (2016).
32. Verbeeck, J., Tian, H. & Van Tendeloo, G. How to manipulate nanoparticles with an electron beam? *Adv. Mater.* **25**, 1114–1117 (2013).
33. Juchtmans, R., Béché, A., Abakumov, A., Batuk, M. & Verbeeck, J. Using electron vortex beams to determine chirality of crystals in transmission electron microscopy. *Phys. Rev. B* **91**, 094112 (2015).
34. Juchtmans, R., Guzzinati, G. & Verbeeck, J. Extension of friedel's law to vortex-beam diffraction. *Phys. Rev. A* **94**, 033858 (2016).
35. Juchtmans, R., Béché, A., Abakumov, A., Batuk, M. & Verbeeck, J. Using electron vortex beams to determine chirality of crystals in transmission electron microscopy. *Phys. Rev. B* **91**, 094112 (2015).
36. Mousley, M., Thirunavukkarasu, G., Babiker, M. & Yuan, J. Robust and adjustable c-shaped electron vortex beams. *N. J. Phys.* **19**, 063008 (2017).
37. Handali, J., Shakya, P. & Barwick, B. Creating electron vortex beams with light. *Opt. Express* **23**, 5236–5243 (2015).
38. Leach, J., Yao, E. & Padgett, M. J. Observation of the vortex structure of a non-integer vortex beam. *N. J. Phys.* **6**, 71–71 (2004).
39. McMorran, B. J. et al. Origins and demonstrations of electrons with orbital angular momentum. *Philos. Trans. R. Soc. A: Math., Phys. Eng. Sci.* **375**, 20150434 (2017).
40. Béché, A., Juchtmans, R. & Verbeeck, J. Efficient creation of electron vortex beams for high resolution stem imaging. *Ultramicroscopy* **178**, 12–19 (2017). FEMMS 2015.
41. Béché, A., Van Boxem, R., Van Tendeloo, G. & Verbeeck, J. Magnetic monopole field exposed by electrons. *Nat. Phys.* **10**, 26–29 (2014).
42. Phatak, C. & Petford-Long, A. Direct evidence of topological defects in electron waves through nanoscale localized magnetic charge. *Nano Lett.* **18**, 6989–6994 (2018).
43. Bliokh, K. Y., Schattschneider, P., Verbeeck, J. & Nori, F. Electron vortex beams in a magnetic field: A new twist on landau levels and aharonov-bohm states. *Phys. Rev. X* **2**, 041011 (2012).
44. Rajabi, A. & Berakdar, J. Relativistic electron vortex beams in a constant magnetic field. *Phys. Rev. A* **95**, 063812 (2017).
45. Han, Y. D. & Choi, T. Classical understanding of electron vortex beams in a uniform magnetic field. *Phys. Lett. A* **381**, 1335–1339 (2017).
46. Grillo, V. et al. Observation of nanoscale magnetic fields using twisted electron beams. *Nat. Commun.* **8**, 689 (2017).
47. Mansuripur, M. Computation of electron diffraction patterns in lorentz electron microscopy of thin magnetic films. *J. Appl. Phys.* **69**, 2455–2464 (1991).
48. McVitie, S. & Cushley, M. Quantitative fresnel lorentz microscopy and the transport of intensity equation. *Ultramicroscopy* **106**, 423–431 (2006).
49. Walton, S. K., Zeissler, K., Branford, W. R. & Felton, S. Malts: A tool to simulate lorentz transmission electron microscopy from micromagnetic simulations. *IEEE Trans. Magn.* **49**, 4795–4800 (2013).
50. Humphrey, E. & De Graef, M. On the computation of the magnetic phase shift for magnetic nano-particles of arbitrary shape using a spherical projection model. *Ultramicroscopy* **129**, 36–41 (2013).
51. Pampaloni, F. & Enderlein, J. Gaussian, hermite-gaussian, and laguerre-gaussian beams: A primer (2004).
52. Kotlyar, V. V. et al. Generation of phase singularity through diffracting a plane or gaussian beam by a spiral phase plate. *J. Opt. Soc. Am. A* **22**, 849–861 (2005).
53. Pohl, D. et al. Atom size electron vortex beams with selectable orbital angular momentum. *Sci. Rep.* **7**, 934 (2017).
54. Beleggia, M. Electron-optical phase shift of a josephson vortex. *Phys. Rev. B* **69**, 014518 (2004).
55. Tonomura, A. et al. Evidence for aharonov-bohm effect with magnetic field completely shielded from electron wave. *Phys. Rev. Lett.* **56**, 792–795 (1986).
56. Aharonov, Y. & Bohm, D. Significance of electromagnetic potentials in the quantum theory. *Phys. Rev.* **115**, 485–491 (1959).
57. Gómez, A. & Castaño, V. M. Unified approach to the high-energy approximation in transmission electron microscopy. *Phys. Status Solidi* **107**, 845–850 (1988).
58. Salesi, G. & Recami, E. A velocity field and operator for spinning particles in (nonrelativistic) quantum mechanics. *Found. Phys.* **28**, 763–773 (1998).
59. Nalewajski, R. F. On probability flow descriptors in position and momentum spaces. *J. Math. Chem.* **53**, 1966–1985 (2015).
60. Jackson, J. D. Classical electrodynamics (Third edition. New York : Wiley, 1999). 785-790.
61. Graef, M. D., Nuhfer, N. T. & McCartney, M. R. Phase contrast of spherical magnetic particles. *J. Microsc.* **194**, 84–94 (1999).
62. Gureyev, T. E. & Nugent, K. A. Phase retrieval with the transport-of-intensity equation. ii. orthogonal series solution for nonuniform illumination. *J. Opt. Soc. Am. A* **13**, 1670–1682 (1996).
63. Zuo, C. et al. Transport of intensity equation: a tutorial. *Opt. Lasers Eng.* **135**, 106187 (2020).
64. Blackburn, A. & Loudon, J. Vortex beam production and contrast enhancement from a magnetic spiral phase plate. *Ultramicroscopy* **136**, 127–143 (2014).
65. Teague, M. R. Image formation in terms of the transport equation. *J. Opt. Soc. Am. A* **2**, 2019–2026 (1985).
66. Lubk, A., Guzzinati, G., Börrnert, F. & Verbeeck, J. Transport of intensity phase retrieval of arbitrary wave fields including vortices. *Phys. Rev. Lett.* **111**, 173902 (2013).
67. Barrows, F., Petford-Long, A. & Phatak, C. Topological defects and interaction of electron waves and localized magnetic charge. *Microsc. Microanalysis* **24**, 940–941 (2018).
68. McVitie, S. Noise considerations in the application of the transport of intensity equation for phase recovery. In Luysberg, M., Tillmann, K. & Weirich, T. (eds.) *EMC 2008 14th European Microscopy Congress 1–5 September 2008, Aachen, Germany*, 771–772 (Springer Berlin Heidelberg, Berlin, Heidelberg, 2008).
69. Lee, Z., Rose, H., Lehtinen, O., Biskupek, J. & Kaiser, U. Electron dose dependence of signal-to-noise ratio, atom contrast and resolution in transmission electron microscope images. *Ultramicroscopy* **145**, 3–12 (2014). Low-Voltage Electron Microscopy.

70. Cooper, D. et al. Medium resolution off-axis electron holography with millivolt sensitivity. *Appl. Phys. Lett.* **91**, 143501 (2007).
71. Linck, M., Freitag, B., Kujawa, S., Lehmann, M. & Niermann, T. State of the art in atomic resolution off-axis electron holography. *Ultramicroscopy* **116**, 13–23 (2012).
72. Lee, H. S., Choe, S. B., Shin, S. C. & Kim, C. G. Characterization of magnetic properties in co/pd multilayers by hall effect measurement. *J. Magn. Magn. Mater.* **239**, 343–345 (2002).
73. Bouard, C. et al. Magnetic properties of perpendicularly magnetized [au/co/pd]n thin films and nanostructures with dzyaloshinskii-moriya interaction. *AIP Adv.* **8**, 095315 (2018).
74. Phatak, C., Petford-Long, A. & De Graef, M. Recent advances in lorentz microscopy. *Curr. Opin. Solid State Mater. Sci.* **20**, 107–114 (2016).
75. Greenberg, A., McMorran, B., Johnson, C. & Yasin, F. Magnetic phase imaging using interferometric stem. *Microsc. Microanalysis* **26**, 2480–2482 (2020).
76. Bisotti, M. A. et al. FinMag: finite-element micromagnetic simulation tool (2018). <https://doi.org/10.5281/zenodo.1216011>.
77. Logg, A., Mardal, K. A., Wells, G. N. et al. Automated Solution of Differential Equations by the Finite Element Method (Springer, 2012).
78. Beleggia, M. et al. Quantitative study of magnetic field distribution by electron holography and micromagnetic simulations. *Appl. Phys. Lett.* **83**, 1435–1437 (2003).

Acknowledgements

This work was supported by the U.S. Department of Energy, Office of Science, Office of Basic Energy Science, Materials Sciences and Engineering Division.

Author contributions

F.B. designed research; F.B. and C.P. developed simulations; F.B., A.P. and C.P. analyzed results and wrote the manuscript; C.P. supervised the project.

Competing interests

The authors declare no competing interests.

Additional information

Supplementary information The online version contains supplementary material available at <https://doi.org/10.1038/s42005-022-01082-z>.

Correspondence and requests for materials should be addressed to Charudatta Phatak.

Peer review information *Communications Physics* thanks Tyler R Harvey and the other, anonymous, reviewer(s) for their contribution to the peer review of this work.

Reprints and permission information is available at <http://www.nature.com/reprints>

Publisher's note Springer Nature remains neutral with regard to jurisdictional claims in published maps and institutional affiliations.



Open Access This article is licensed under a Creative Commons Attribution 4.0 International License, which permits use, sharing, adaptation, distribution and reproduction in any medium or format, as long as you give appropriate credit to the original author(s) and the source, provide a link to the Creative Commons license, and indicate if changes were made. The images or other third party material in this article are included in the article's Creative Commons license, unless indicated otherwise in a credit line to the material. If material is not included in the article's Creative Commons license and your intended use is not permitted by statutory regulation or exceeds the permitted use, you will need to obtain permission directly from the copyright holder. To view a copy of this license, visit <http://creativecommons.org/licenses/by/4.0/>.

© UChicago Argonne, LLC, Operator of Argonne National Laboratory 2022